Magnetic imaging of spin waves and magnetic phase transitions with nitrogen-vacancy centers in diamond

Bertelli, I.

Citation

Bertelli, I. (2021, November 24). *Magnetic imaging of spin waves and magnetic phase transitions with nitrogen-vacancy centers in diamond*. *Casimir PhD Series*. Retrieved from https://hdl.handle.net/1887/3245183

2

NV MAGNETOMETRY

Nitrogen-vacancy (NV) centers are atomic defects in diamond, whose electronic spin can be controlled and readout with a combination of optical and microwave excitation. Their non-invasive character and sensitivity to GHz magnetic fields makes them well suited to study the dynamic excitations of magnetic systems, such as spin waves. In Chapters 4-7 we use these sensors to study thermal and coherent spin waves, and to characterize a meta-magnetic phase transition. In this chapter we discuss the properties of NV centers that are required to understand these experiments.

This chapter is divided into two parts. In the first part (Section 2.1) we introduce the physics and working principles of nitrogen-vacancy centers in diamond, concluding with a description of the confocal microscope used to optically detect them. In the second part (Section 2.2) we consider an NV center in a magnetic field and express its Hamiltonian in a form that is useful to understanding Chapter 3 and the results of Chapters 6-5 (Section 2.2.1). We then explain how NV centers can be used as sensors of static (Section 2.2.2), coherently oscillating (Section 2.2.3-2.2.4) and incoherent (Section 2.2.5) magnetic fields. All these measurement techniques are the foundation upon which the results of this thesis are built. We conclude with a description of the electronic setup used to control and detect the NV spin state (Section 2.2.6).

2.1. NV CENTERS IN DIAMOND

Several extensive reviews treat the physics of NV centers in depth [1–3]. In this section we briefly describe the electronic structure of an NV center and how this is related to its spin-dependent optical properties, starting point of understanding the working principles of NV magnetometry.

2.1.1. ELECTRONIC STRUCTURE

Nitrogen-vacancy (NV) centers are point defects in the diamond lattice consisting of a substitutional nitrogen atom adjacent to a missing carbon atom (Fig. 2.1a). They can occur with the N-V axis oriented along any of the four $\langle 111 \rangle$ directions of the diamond lattice. This defect has a C_{3V} symmetry with axis along the N-V direction and can exist in the neutral NV^0 or charged NV^- states [4]. The electronic structure of NV^0 is composed of five unpaired electrons, two from the nitrogen and three from the carbon atoms nearest-neighbour to the vacancy [5, 6]. An additional electron can be trapped by the defect, resulting in NV^- [6]. This charge state is the one typically used for sensing applications because of its photophysics (see next section). In the rest of this thesis we focus exclusively on the negatively charged state and simply denote it "NV", for clarity.

The energy level scheme of NV centers (Fig. 2.1b) consists of triplet ground and excited states and intermediate singlet states [7][1]. Both $S = 1$ triplet levels are split into $m_s = |0\rangle$ and $m_s = |\pm 1\rangle$ states (where m_s indicates the spin projection along the NV quantization axis) by the spin-spin interaction, resulting in a ground (excited) state zero-field splitting $D \approx 2.87$ GHz ($D_{ES} \approx 1.42$ GHz).

2.1.2. SPIN-DEPENDENT OPTICAL PROPERTIES

Among many existing lattice defects, NV centers in diamond have gained importance for sensing because of the relation between their spin and optical properties [10].

The photoluminescence emission spectrum of NVs (Fig. 2.1c) shows a zero-phonon line (ZPL) at 637 nm and a broad phonon sideband (PSB). The PSB is related to transitions in which one phonon is excited/absorbed in addition to a photon at the ZPL. Thus, the PSB allows the non-resonant optical excitation with a green laser. Once excited, the NV can relax either through a spin-conserving optical transition or non-radiatively by intersystem crossing (ISC) via the singlet states.

The $m_s = |0\rangle$ state has a lower ISC shelving rate to the singlet states than $m_s = |\pm 1\rangle$ [7, 11]. Additionally, the singlet states preferentially decay toward $m_s = |0\rangle$ [2]. These spin-selective processes have the net effect of populating the $m_s = |0\rangle$ state to a high degree upon optical pumping, which allows for optical initialization into $m_s = |0\rangle$. For the same reasons, the optical transition is significantly brighter when the spin is in the $m_s = |0\rangle$ state. This spin-dependent photoluminescence forms the basis for the optical detection of the NV spin state, upon which a large part of the field of NV magnetometry

---

[1] The number of singlet states has not been determined clearly, with predictions and experiments reporting between two [8] and three [9], but the actual number can be generally neglected to the purpose of NV magnetometry.

is built [1–3, 12].

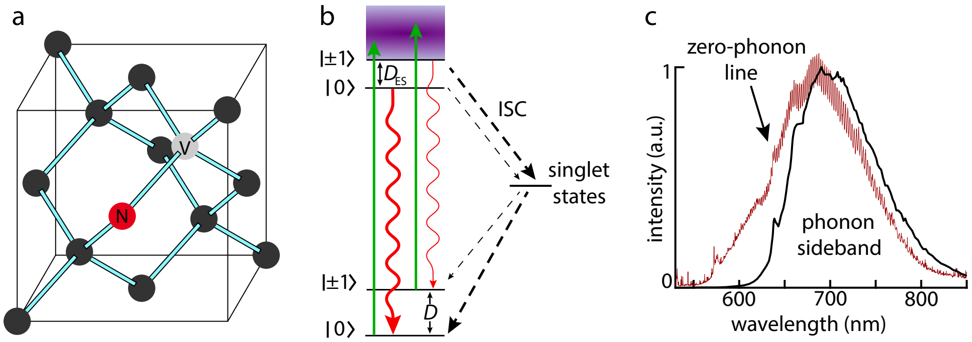

Figure 2.1: Structural, electronic and optical properties of NV centers. (**a**) Atomic structure of an NV defect in the diamond lattice. Carbon atoms are represented as dark grey spheres, while the vacancy (nitrogen atom) is represented as a light gray (red) sphere. (**b**) Energy level scheme of an NV center. The zero-field splitting in the ground (excited) state is D = 2.87 GHz (D_{ES} = 1.4 GHz) at room temperature. The green arrows represent spin-conserving non-resonant optical excitation with a green laser (515 nm) from the ground states to the phonon sideband (shaded in purple). The red wiggly arrows indicate decay via spin-conserving optical transitions, while the black dashed lines indicate non-radiative relaxation paths via inter-system crossing (ISC). The weight of the lines indicates the relative strength of the transition. (**c**) Photoemission spectrum of NV centers. Red line: spectrum of the NV ensemble used for the measurements of Chapter 4-5 and 7, measured with green excitation at 515 nm. Black line: spectrum of reference NV$^-$ center [13], showing a zero-phonon line (ZPL) at 637 nm and a broad phonon sideband between 650 and 800 nm. The additional luminescence of the NV ensemble compared to the reference NV$^-$ is attributed to the presence of centers in the netural NV^0 state.

2.1.3. DETECTING NV CENTERS: CONFOCAL MICROSCOPY

One way of optically addressing single NV centers is with a confocal microscope [14]. A sketch of one of the two confocal microscopes built to perform the experiments in this thesis is shown in Fig. 2.2a. A green laser beam (wavelength 515 nm) is focused to a diffraction-limited spot by an objective with high numerical aperture (NA=0.95, typically). The excited NV center emits photoluminescence (PL), which is collected via the same objective and separated from the green excitation by a dichroic mirror and optical filters. The PL is successively focused through a pinhole (diameter 50 μm) before being focused on the sensor of an avalanche photodiode (APD) with ≤ 250 dark counts per second. The pinhole ensures that only light emitted from a point in a confocal plane can reach the APD. Blocking the out-of-focus light increases the signal-to-background ratio, allowing for the detection of single NV centers (Fig. 2.2b).

The second setup built (with a heating sample-stage, used for the experiments of Chapter 7) employs a fiber-coupled Si-PIN photodiode, instead of an APD. The photodiode

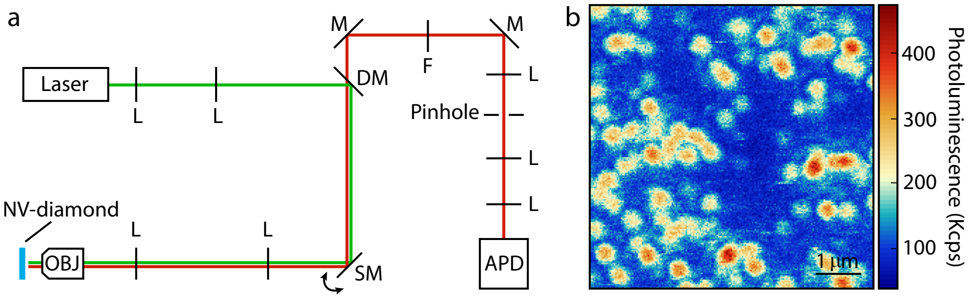

Figure 2.2: Detecting single NV centers with confocal microscopy. **a**) Sketch of the setup. A laser (*Cobolt 06-MLD 515 nm*) emits green light toward a dichroic mirror (DM, cutoff at 607 nm) after passing through a beam expander composed of two lenses (L). The dichroic mirror reflects the green light, which reaches a scanning mirror (*Thorlabs GVS212/M*) and the NV-diamond after a second beam-expander and a large-NA objective (*Olympus MPlanApo 50X*, NA=0.95). The NV centers emit broadband red light that is collected by the same objective and follows the excitation path backward until the dichroic mirror, where it is transmitted to the APD single-photon counting module(*Excelitas SPCM-AQRH-13* and successively *Laser Components COUNT-NIR-100*) after being filtered (F, long-pass) focused through the pinhole (diameter 50 µm). (**b**) Photoluminescence image of a diamond containing single NV centers, visible as high-PL circular spots.

has a dark current that corresponds to a higher background signal, but also much higher saturation power, which is well suited to working with ensembles of NVs. No pinhole is used because the core of the multimode optical fiber (diameter ~ 50 µm) spatially filters the incoming light in a similar way.

2.2. MAGNETIC FIELD SENSING WITH NV CENTERS

In this section we describe how to sense static and oscillating magnetic fields using NV centers. We start by expressing the NV center Hamiltonian in a magnetic field in a form that is useful to the remainder of this thesis (Section 2.2.1). We then discuss the electron spin resonance (ESR) technique, used to characterize static fields and to probe the power of the microwave field driving the NV center (Section 2.2.2). Afterwards, we introduce the idea of a rotating reference frame (Section 2.2.3), which introduces the idea that a circularly-polarized magnetic field of a certain handedness only drives one of the two NV ground-state transitions. Additionally, analyzing the action of oscillating fields in the rotating frame makes it easier to understand pulsed measurement schemes, used to induce Rabi oscillations (Section 2.2.4) and perform T_1 relaxometry (Section 2.2.5). In the rest of this thesis, we use both kind of measurements to detect and characterize GHz oscillating fields. In Section 2.2.6 we show the electronics setup that allows to manipulate and probe the NV spin state.

2.2.1. NV CENTER IN A MAGNETIC FIELD

Both ground and excited states are spin triplets with zero-field splitting between $|0\rangle$ and $|\pm 1\rangle$ states. In a static magnetic field **B**, the $m_s = |-1\rangle$ and $m_s = |+1\rangle$ are additionally split because of the Zeeman interaction [15], so that the NV center energy spectrum in the electronic ground state is determined by the Hamiltonian (in a reference frame with z along the NV axis)[2]

$$\mathcal{H} = DS_z^2 + \gamma \mathbf{B} \cdot \mathbf{S} \tag{2.1}$$

where $\gamma = 2\pi \cdot 28$ MHz/mT is the electronic gyromagnetic ratio and $\mathbf{S} = \left[S_x, S_y, S_z\right]$ are the Pauli spin operators for a spin-1 system, with

$$S_x = \frac{1}{\sqrt{2}} \begin{pmatrix} 0 & 1 & 0 \\ 1 & 0 & 1 \\ 0 & 1 & 0 \end{pmatrix}, \quad S_y = \frac{1}{\sqrt{2}} \begin{pmatrix} 0 & -i & 0 \\ i & 0 & -i \\ 0 & i & 0 \end{pmatrix}, \quad S_z = \begin{pmatrix} 1 & 0 & 0 \\ 0 & 0 & 0 \\ 0 & 0 & -1 \end{pmatrix}. \tag{2.2}$$

Substituting these in Eq. 2.1, we obtain the Hamiltonian in matrix form:

$$\mathcal{H} = \begin{pmatrix} D + \gamma B_z & \frac{\gamma}{\sqrt{2}}(B_x - iB_y) & 0 \\ \frac{\gamma}{\sqrt{2}}(B_x + iB_y) & 0 & \frac{\gamma}{\sqrt{2}}(B_x - iB_y) \\ 0 & \frac{\gamma}{\sqrt{2}}(B_x + iB_y) & D - \gamma B_z \end{pmatrix}. \tag{2.3}$$

A static magnetic field that is oriented exactly along the NV z axis causes a linear shift of the two ESR frequencies $\omega_\pm = D \pm \gamma B_z$. At the same field, NV centers belonging to different families show a different shift (Fig. 2.3a), because they experience a transverse field. Diagonalizing the Hamiltonian yields its eigenvalues ($\lambda_{i=1,2,3}$), from which the ESR frequencies can be determined as $\omega_{+(-)} = \lambda_1 - \lambda_{2(3)}$. These frequencies can be experimentally detected by measuring the electron spin resonance (ESR) spectrum (next section).

Let us now rewrite the Hamiltonian in a form that is useful when considering oscillating fields (Section 2.2.3). Because the $|-1\rangle \leftrightarrow |+1\rangle$ transition is dipole-forbidden[3], we can treat the three-level system of Eq. 2.3 as two effective two-level systems (selecting the upper-left or bottom-right corners of the matrix). The full Hamiltonian can then be rewritten using the spin-1/2 Pauli matrices $\boldsymbol{\sigma} = (\sigma_x, \sigma_y, \sigma_z)$[4] as

$$\mathcal{H}_\pm = \frac{\omega_\pm}{2}(I \pm \sigma_z) + \frac{\gamma}{\sqrt{2}}(B_x\sigma_x + B_y\sigma_y) \tag{2.4}$$

where I is the identity matrix.

2.2.2. ELECTRON SPIN RESONANCE

When performing an NV-based measurement, we usually start by detecting and characterizing the strength and direction of the static field at the NV location. This is done

---

[2] We neglect strains and electric fields, which lead to additional terms in the Hamiltonian [3, 16, 17]. We neglect these effects because they play a minor role for the relatively large magnetic fields considered in this thesis.

[3] These states are coupled by quadrupolar magnetic fields, dipolar electric fields, and mechanical strain [18–21].

[4] $\sigma_x = \begin{pmatrix} 0 & 1 \\ 1 & 0 \end{pmatrix}, \sigma_y = \begin{pmatrix} 0 & -i \\ i & 0 \end{pmatrix}, \sigma_z = \begin{pmatrix} 1 & 0 \\ 0 & -1 \end{pmatrix}$.

by determining the electron spin resonance (ESR) transitions of the NV center(s) used for sensing. Characterizing the ESR transitions is also the first step of any procedure to probe oscillating fields, because knowing the resonances allows to apply microwave pulses of the appropriate frequencies. Additionally, the contrast of ESR transitions provides information regarding the strength of the oscillating field that is resonantly driving the NV center.

DETECTION OF A STATIC FIELD

Transitions between $m_s = |0\rangle$ and $m_s = |\pm 1\rangle$ (both in the ground and excited states) can be induced by a GHz magnetic field that is resonant with an ESR transition $\omega_\pm$ (we study this in detail in Section 2.2.3). In the easiest implementation, an ESR experiment consists of the simultaneous and continuous excitation with light and microwaves[5], of which the frequency is varied, while the emitted photons are collected. When the drive frequency is resonant with either of the ESR transitions, the NV spin is driven from the bright $|0\rangle$ into the dark $|\pm\rangle$ states, such that the NV photoluminesce is reduced. Typical ESR spectra are shown in Fig. 2.3b-c for single NVs and NV ensembles, respectively.

We perform ESR experiments in order to determine the strength and orientation of a static magnetic field at the NV location, by inverting Eq. 2.1. The resulting magnetic field components parallel ($B_\parallel$) and perpendicular ($B_\perp$) to the N-V axis can be written as [23]

$$B_\parallel = \frac{\sqrt{-(D+\omega_+-2\omega_-)(D+\omega_--2\omega_+)(D+\omega_++\omega_-)}}{3\gamma\sqrt{3D}}, \tag{2.5}$$

$$B_\perp = \frac{\sqrt{-(2D-\omega_+-\omega_-)(2D-\omega_++2\omega_-)(2D-\omega_-+2\omega_+)}}{3\gamma\sqrt{3D}}. \tag{2.6}$$

The angle between the NV axis and the field can thus be calculated as $\theta = \arctan(B_\perp/B_\parallel)$.

The procedure of extracting the field strength and angle is used in Chapter 7 to detect local magnetic field variations due to the presence of magnetic domains and domain walls. It is also used to calibrate the magnetic field at the NV location (since we always apply the bias field with a small permanent magnet) whenever a new sample is mounted in the setup.

CHARACTERIZATION OF THE OSCILLATING FIELD MAGNITUDE

The width and contrast of each ESR dip in the spectrum are influenced by several parameters, which include the power of the optical and microwave excitation and the lifetime of the energy levels. The contrast C of an ESR dip can be expressed as [24]

$$C = C_0\frac{B^2_{AC,\perp}}{B^2_{AC,\perp}+\Phi} \tag{2.7}$$

---

[5] ESR can also be measured with a pulsed scheme ("dark ESR") in order to avoid broadening of the transitions induced by the continuous laser excitation [22].

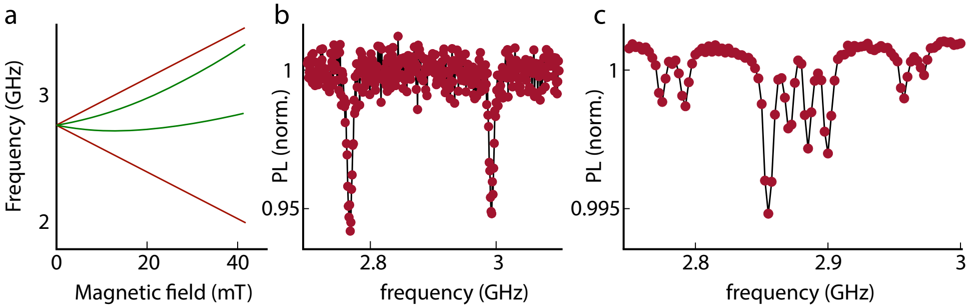

Figure 2.3: Electron spin resonance. (**a**) Magnetic field-evolution of the eight ESR transitions of an NV ensemble. When the field is oriented exactly along one NV family (red lines), the other three families are degenerate because they experience the same misaligned field (green lines). (**b**) ESR spectrum of a single NV center for $B_{\parallel} \sim 4$ mT, $B_{\perp} \sim 5$ mT. (**c**) ESR spectrum of an NV ensemble for a field misaligned with all four NV families. $(B_x, B_y, B_z) \approx (0.6(1), 4.0(1), 0.5(1))$ mT.

where C_0 is the maximum attainable contrast of an ESR transition (roughly $20-25\%$ for single NVs and $2-3\%$ for ensembles), B_{AC} is the amplitude of the magnetic field oscillating at the ESR frequency, perpendicular to the NV axis, and Φ is a parameter that depends on the optical excitation and relaxation time of the NV spin[6]. For small microwave power, when all other parameters are constant, the contrast is a sensitive tool to characterize variations of the strength of the oscillating field. In Chapters 4 and 5 we use this property to spatially image the stray field of spin waves. To obtain quantitative results, we measure Rabi oscillations instead (Section 2.2.4).

2.2.3. DETECTING OSCILLATING FIELDS: THE ROTATING FRAME

In this section we transform the NV Hamiltonian into a rotating frame of reference. This treatment shows that the two NV ESR transitions are driven by circularly-polarized magnetic fields of opposite handedness. Additionally, because it removes the time dependence from the Hamiltonian, it facilitates the understanding of the complex motion of a spin subject to both a static and an oscillating field .

We define a rotating wavefunction $\psi_{R_\pm} = e^{\pm i\omega t\sigma_z/2}\psi$, and use the time-dependent Schrödinger's equation

$$i\hbar\frac{\partial\psi}{\partial t} = \mathcal{H}\psi \tag{2.8}$$

to obtain

$$\frac{\partial\psi}{\partial t} = e^{\mp i\omega t\sigma_z/2}\frac{\partial\psi_{R_\pm}}{\partial t} \mp i\omega\sigma_z\psi_{R_\pm}/2 = -\frac{i}{\hbar}\mathcal{H}e^{\mp i\omega t\sigma_z/2}\psi_{R_\pm}. \tag{2.9}$$

---

[6] For typical values of the T_1 and T_2^* relaxation rates and optical power P_{opt}, $\Phi = \frac{2}{\gamma}\Gamma_p\Gamma_c$, where Γ_p (Γ_c) is the optically-induced polarization (relaxation) rate [24]. They both depend on $s = P_{\text{opt}}/P_{\text{sat}}$ as $\Gamma_{p(c)} = \Gamma^{\infty}_{p(c)}\left(\frac{s}{s+1}\right)$, where P_{sat} is the optical power at saturation of the NV luminescence (i.e. half of the maximum attainable PL) and $\Gamma^{\infty}_{p(c)}$ is the polarization (relaxation) rate at saturation [24]. Depending on the optical power P_{opt}, $\Phi \approx 10^{13} - 10^{14}$ Hz [24].

Rewriting this, we can obtain a new Schrödinger's equation for the rotating wavefunction:

$$\frac{\partial \psi_{R_\pm}}{\partial t} = -i(e^{\pm i\omega t\sigma_z/2}\mathscr{H}e^{\mp it\sigma_z/2} \mp \omega\sigma_z/2)\psi_{R_\pm} = -\frac{i}{\hbar}\mathscr{H}_{R_\pm}\psi_{R_\pm}. \tag{2.10}$$

Thus, the new Hamiltonian in the frame that is rotating synchronously with the wavefunction is given by

$$\mathscr{H}_{R_\pm} = e^{\pm i\omega t\sigma_z/2}\mathscr{H}e^{\mp i\omega t\sigma_z/2} \mp \omega\sigma_z/2. \tag{2.11}$$

We can now analyze the NV center in a static field (along the z axis) and consider what happens when we apply an oscillating field in the xy plane. Such transverse field can generally be elliptically polarized, such that it can be written as sum of two counter-rotating circular components of amplitude B_R and $B_{R'}$:

$$\begin{aligned} B_{AC} &= \frac{1}{\sqrt{2}}B_R\left[\cos(\omega t)\sigma_x + \sin(\omega t)\sigma_y\right] + \frac{1}{\sqrt{2}}B_{R'}\left[\cos(\omega t)\sigma_x - \sin(\omega t)\sigma_y\right] && (2.12)\\ &= \frac{1}{\sqrt{2}}\cos(\omega t)\sigma_x(B_R + B_{R'}) + \frac{1}{\sqrt{2}}\sin(\omega t)\sigma_y(B_R - B_{R'}). && (2.13) \end{aligned}$$

We can transform the two-level Hamiltonian (Eq. 2.4) in the rotating frame, using Eq. 2.11

$$\mathscr{H}'_\pm = e^{\pm i\omega t\sigma_z/2}\mathscr{H}_\pm e^{\mp i\omega t\sigma_z/2} \mp \omega\sigma_z/2 = \frac{I\omega_\pm}{2} \mp \frac{\sigma_z\Delta_\pm}{2} + e^{\pm i\omega t\sigma_z/2}(\gamma B_{AC})e^{\mp i\omega t\sigma_z/2}, \tag{2.14}$$

where $\Delta_\pm = \omega - \omega_\pm$ is the detuning between the NV transition and the drive field. Working out the matrix products, we obtain

$$\begin{aligned} \mathscr{H}'_+ &= \frac{I\omega_+}{2} + \frac{1}{\sqrt{2}}B_R\sigma_x + \frac{1}{\sqrt{2}}B_{R'}\left[\sigma_x\cos(2\omega t) - \sigma_y\sin(2\omega t)\right] - \frac{\sigma_z\Delta_+}{2}, && (2.15)\\ \mathscr{H}'_- &= \frac{I\omega_-}{2} + \frac{1}{\sqrt{2}}B_{R'}\sigma_x + \frac{1}{\sqrt{2}}B_R\left[\sigma_x\cos(2\omega t) + \sigma_y\sin(2\omega t)\right] + \frac{\sigma_z\Delta_-}{2}. && (2.16) \end{aligned}$$

For $\mathscr{H}'_+$ ($\mathscr{H}'_-$), when $|2\omega - \Delta_+| \gg B_R$ ($|2\omega - \Delta_-| \gg B_{R'}$) we can disregard the terms oscillating at 2ω (rotating wave approximation [25])[7], such that the spin dynamic in the new frame is driven by the $B_{R(R')}$ component, which appears static in the frame rotating at $+\omega(-\omega)$ (Fig. 2.4).

Importantly, Eqs. 2.15-2.16 show that the $\omega\pm$ transitions are driven by circularly-polarized magnetic fields of opposite handedness. This turns out to be crucial to the detection and characterization of spin waves of Chapters 4-6, because they generate fields that are circularly polarized (see Chapter 3 for the derivation of spin-wave stray fields), so that spin waves propagating to the right (left) drive almost exclusively the $|0\rangle \leftrightarrow |-1\rangle$ ($|0\rangle \leftrightarrow |+1\rangle$) transition.

Since each transition is driven by a circularly-polarized field of a certain handedness, a linearly-polarized field (such as that of a wire or a microstrip) drives both transitions equally, because it can be expressed as the sum of two counter-rotating circular components.

---

[7] These components only cause minor modifications, known as Bloch-Siegert effects [26, 27], which are only relevant when the amplitude of the oscillating field is strong compared to its detuning from the ESR transition.

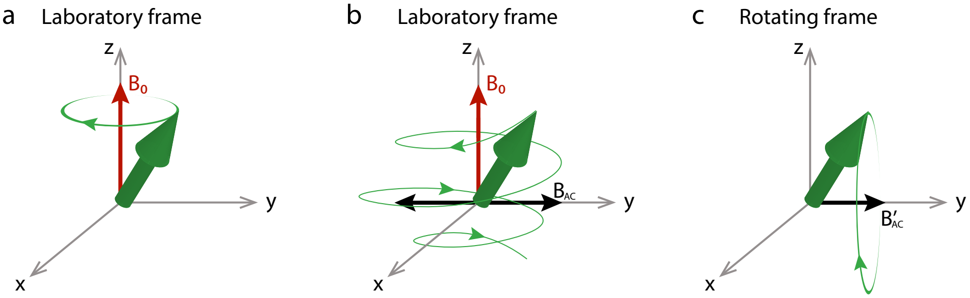

Figure 2.4: Electron spin in a magnetic field. (**a**) In the laboratory frame, an electron spin subjected to a static magnetic field precesses around it. (**b**) When a resonant oscillating field is applied in the transverse plane, the spin rotates around the vector sum of the two fields, following a complicated trajectory. (**c**) In a reference frame rotating at the same frequency of the spin and transverse field, the trajectory is much simpler: the spin "Rabi" precesses around the transverse field, which in this frame appears static.

2.2.4. RABI OSCILLATIONS

We see from Eqs. 2.15-2.16 that B_R ($B_{R'}$) has become static in the rotating frame. As such, this transverse field drives "Rabi" oscillations [28, 29] with frequency

$$\Omega_\pm = \sqrt{\Omega_R^2 + \Delta_\pm^2}, \tag{2.17}$$

where $\Omega_R = \gamma B_{R(R')}/\sqrt{2}$. At resonance (i.e. $\Delta_\pm = 0$), $\Omega = \Omega_{R(R')}$. To ensure resonance between the ESR transition and the applied oscillating field, we always perform an ESR measurement before exciting Rabi oscillations. However, when the Rabi frequency is below ~ 5 MHz, we must take into account that the ESR transition is actually split in two transitions (separated by ~ 3 MHz) by the nuclear hyperfine interaction of the nitrogen atoms used to create the NV center by ^{15}N implantation [30]. Thus, the field we apply is detuned from each hyperfine-split transition by ~ 1.5 MHz. This situation occurs in Chapter 4 (Fig. 4.2).

Measuring Rabi oscillations allows to quantify $B_{R(R')}$, i.e. the amplitude of the oscillating field driving NV centers. We can perform a Rabi measurement using the pulsed control scheme shown in Fig. 2.5a. Microwave bursts of increasing duration rotate the NV spin between the $|0\rangle$ (high luminescence) and the $|\pm 1\rangle$ states (Fig. 2.5b). We calculate the Rabi frequency from the period of the luminescence oscillations.

Knowing the Rabi frequency, we can calibrate the duration of a microwave burst that would prepare the NV spin in the $|-1\rangle$ or $|+1\rangle$ state (known as π pulse because, in the rotating frame, a spin prepared along $= z$ rotates by an angle π until $-z$) by choosing a pulse length that corresponds to the first minimum in the Rabi oscillation measurement (Fig. 2.5). Similarly, a $\pi/2$ pulse brings the spin on the xy plane, where the spin

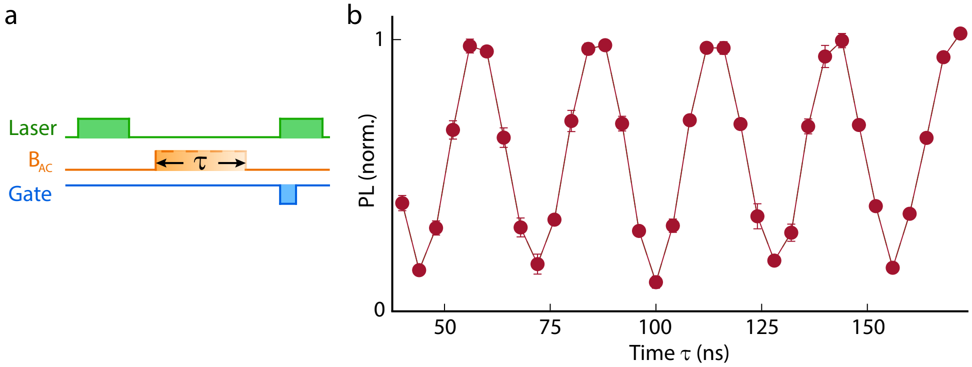

Figure 2.5: Rabi oscillations measurement. (**a**) Pulse sequence used to measure Rabi oscillations. Green laser pulses are used to initialize and read out the NV spin state. A resonant microwave burst of variable duration τ induces Rabi rotations of the NV spin. The emitted photons are counted during the first 400 ns of the second laser pulse. (**b**) Typical result of a Rabi oscillation experiment. As a function of the microwave pulse length, the NV spin state rotates between the $|0\rangle$ (high PL) and the $|\pm 1\rangle$ (low PL) states. The signal does not start from 1 because the first pulse has non-zero duration (~ 40 ns).

is dephased by slow variations of the static field[8] or, in the case of NV ensembles, local field variations over the detection volume (i.e. the laser spot with size determined by the diffraction limit).

We use pulsed control of the NV spin in Chapter 4 in a time-of-flight experiment on spin waves and in Chapter 6 to characterize the longitudinal relaxation time of the NV spin (this kind of measurements is known as "relaxometry").

2.2.5. T_1 RELAXOMETRY

Measuring Rabi oscillations allows the calibration of the duration of pulses used to deterministically prepare the NV spin in any coherent state. Measuring the time evolution of coherent states enables to characterize the source of the magnetic field responsible for the system dynamics. Advanced sequences of $\pi/2$ and π pulses can be used to, e.g., selectively lock-in to a magnetic field of a certain frequency while filtering out all other components [10, 31–37], deterministically enable or disable the influence of a system on the probe [38–41], and characterize dephasing and decoherence processes [38, 42].

In this thesis, we employ π pulses to measure the velocity of spin waves (Chapter 4) and the longitudinal NV relaxation rate as a result of magnetic-noise-induced decoherence

---

[8] Here, fields are "slow" when they are quasi-static, i.e. almost constant during a single measurement but varying over many repetitions. Some examples are the effective field due to the statistical polarization of the spins in the NV environment, such as the nuclear spins of the neighbouring ^{13}C atoms, as well as the electron spins of other substitutional nitrogen atoms [43].

(Chapter 6). The measurement protocol for the NV relaxation rate simply consists of preparing the NV spin in one of the three eigenstates and monitoring how long it takes to relax to the stationary situation (i.e. the NV spending 1/3 of time in each state). We prepare the spin in $|0\rangle$ by optical pumping. We apply a subsequent π pulse on the $\omega_\pm$ transition to flip the spin into the $|\pm 1\rangle$ states. The pulse sequence is shown in Fig. 2.6a.

The NV-spin relaxation dynamics can be described by a rate-equation model, where the time-evolution of the population $\mathbf{P}(t)$ of the three ground states can be expressed as [23, 44]

$$\frac{d\mathbf{P}(t)}{dt} = \mathbf{\Gamma}\mathbf{P}(t) = \begin{pmatrix} -(\Gamma_{-1,0}+\Gamma_{-1,+1}) & \Gamma_{0,-1} & \Gamma_{+1,-1} \\ \Gamma_{-1,0} & -(\Gamma_{0,-1}+\Gamma_{0,+1}) & \Gamma_{+1,0} \\ \Gamma_{-1,+1} & \Gamma_{0,+1} & -(\Gamma_{+1,0}+\Gamma_{+1,-1}) \end{pmatrix} \mathbf{P}(t) \qquad (2.18)$$

where $\Gamma_{i,j} = \Gamma_{j,i}$ is the transition rate between states $|i\rangle$ and $|j\rangle$ and we set $\Gamma_{-1,+1} = 0$ because magnetic field noise does not directly couple these states (see previous section). The system dynamics is therefore described by only two rates ($\Gamma_{0,-1} := \Gamma_-$ and $\Gamma_{0,+1} := \Gamma_+$):

$$\mathbf{\Gamma} = \begin{pmatrix} -\Gamma_- & \Gamma_- & 0 \\ \Gamma_- & -(\Gamma_- + \Gamma_+) & \Gamma_+ \\ 0 & \Gamma_+ & -\Gamma_+ \end{pmatrix}. \qquad (2.19)$$

Fig. 2.6b shows a typical relaxation measurements of the three spin states in a system where $\Gamma_- \neq \Gamma_+$. Measuring the time-relaxation of the three states and fitting the data to the model (Eq.2.20) allows to extract the two relaxation rates $\Gamma_\pm$.

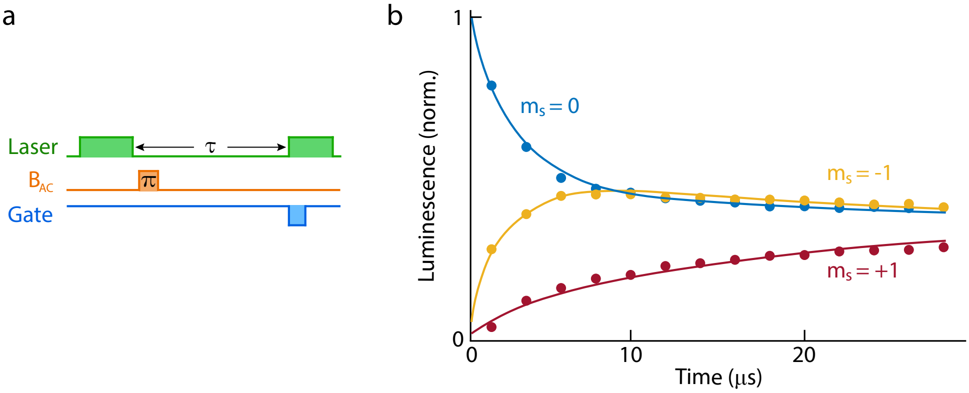

Figure 2.6: Relaxation measurement. (**a**) Pulse sequence for a relaxometry measurement. A green laser pulse prepares the NV spin in the $|0\rangle$ state. A π pulse (on either transition) can prepare the NV spin in the ± 1 states. After a waiting time τ, the spin state is read out during the first 400 ns of a laser pulse. (**b**) Typical NV relaxation measurement of the three states. In this case, the relaxation rate Γ_- is much larger than Γ_+ (data from Chapter 6).

The relaxation rates can be expressed in term of field-field correlators[9]. We start from

---

[9] In this thesis we only consider magnetic noise generated by the fluctuations of the magnetic field of thermally-

Eq. 2.4, considering a static field along the NV z axis and a resonant field oscillating in the xy plane. Using linear perturbation theory, the relaxation rates are given by [23, 46–49]

$$\Gamma_{\pm} = \frac{\gamma^2}{2} \int_{-\infty}^{+\infty} \mathrm{d}t e^{i\omega_{\pm} t} \langle B_{\pm}(t) B_{\mp}(0) \rangle \,. \tag{2.20}$$

where $\langle \ldots \rangle$ indicates ensemble averaging over the realizations of the field fluctuations.

In Chapter 3 we derive the NV relaxation rates caused by thermally-excited incoherent magnons, which generate magnetic fluctuations at the $\omega_{\pm}$ ESR frequencies and result in a large increase of the NV relaxation rates.

2.2.6. CONTROLLING NV CENTERS: SETUP ELECTRONICS

The oscillating magnetic field used to induce NV spin transitions in the ground state is generated inductively, throughout this thesis, by current running through a wire (i.e. a bonding wire pushed close to the sample, as in Chapters 4, 6, 7) and/or a Ti/Au microstrip fabricated on a magnetic substrate (as in Chapters 4 and 5). This microwave current is generated by two microwave sources and amplified, if necessary. A programmable pulse generator controls the timing of such microwave bursts, of the laser excitation, and of the readout window. Additionally, the pulse generator triggers the data acquisition by the data-acquisition card (DAQ). Fig. 2.7 shows the electronic elements and connections of the setup.

---

excited spin waves. In magnetic systems, these fluctuations are typically much larger than other components. In non-magnetic systems, the dominating noise source can be electronic transport [45].

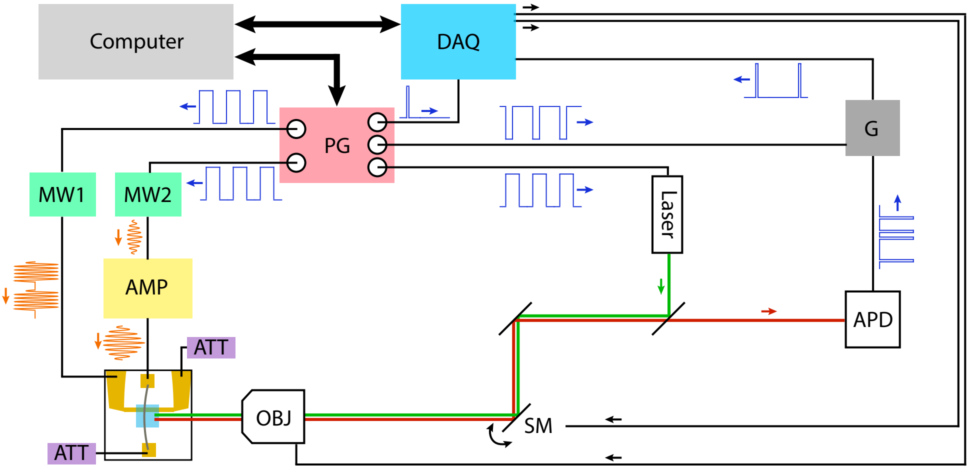

Figure 2.7: Sketch of the electronic setup. The whole electronic setup is controlled via a computer (top left corner), that communicates with a National Instrument data-acquisition (DAQ) card (*NI PCIe-6343*). This card supplies DC voltages to control the scanning mirror (SM), the in-plane sample position and the piezo-actuated stage (*PIFOC Piezo X-drive*) that controls the distance between the objective (OBJ) and the sample. Additionally, the DAQ card is used to count the pulses generated by the avalanche photodetector (APD) when a photon is collected. Before reaching the DAQ card, such pulses pass through a pull-up resistor (G, for "gate"). When the "counter gate" output of the pulse generator (PG, *PulseBlasterESR-PRO-500*) is low (high) the APD pulses (don't) reach the counter on the DAQ card. Additionally, the PG generates pulses to trigger data acquisition (the DAQ card stores counts until a new trigger is received), and controls the laser and two microwave sources (MW1 and MW2, both *Rohde & Schwarz SGS100A*). The signal from MW1 typically reaches a microstrip on the sample, while the one from MW2 reaches a bonding wire after being amplified by a high-power broadband amplifier (*AR 30 W 1-6 GHz*). After reaching the sample, each microwave channel is terminated with a 50 Ω-impedance attenuator and terminator.

REFERENCES

[1] M. W. Doherty, N. B. Manson, P. Delaney, F. Jelezko, J. Wrachtrup, and L. C. Hollenberg, *The nitrogen-vacancy colour centre in diamond,* Physics Reports **528**, 1 (2013).

[2] L. Rondin, J. P. Tetienne, T. Hingant, J. F. Roch, P. Maletinsky, and V. Jacques, *Magnetometry with nitrogen-vacancy defects in diamond,* Reports on Progress in Physics **77**, 056503 (2014).

[3] R. Schirhagl, K. Chang, M. Loretz, and C. L. Degen, *Nitrogen-Vacancy Centers in Diamond: Nanoscale Sensors for Physics and Biology,* Annual Review of Physical Chemistry **65**, 83 (2014).

[4] Y. Mita, *Change of absorption spectra in type-Ib diamond with heavy neutron irradiation,* Physical Review B **53**, 11360 (1996).

[5] J. H. Loubser and J. A. Van Wyk, *Electron spin resonance in the study of diamond,* Reports on Progress in Physics **41**, 1201 (1978).

[6] M. W. Doherty, N. B. Manson, P. Delaney, and L. C. L. Hollenberg, *The negatively charged nitrogen-vacancy centre in diamond: the electronic solution,* New Journal of Physics **13**, 25019 (2011).

[7] L. Robledo, H. Bernien, T. Van der Sar, and R. Hanson, *Spin dynamics in the optical cycle of single nitrogen-vacancy centres in diamond,* New Journal of Physics **13**, 025013 (2011).

[8] V. M. Acosta, E. Bauch, M. P. Ledbetter, A. Waxman, L. S. Bouchard, and D. Budker, *Temperature dependence of the nitrogen-vacancy magnetic resonance in diamond,* Physical Review Letters **104**, 070801 (2010).

[9] Y. Ma, M. Rohlfing, and A. Gali, *Excited states of the negatively charged nitrogen-vacancy color center in diamond,* Physical Review B **81**, 041204 (2010).

[10] C. L. Degen, F. Reinhard, and P. Cappellaro, *Quantum sensing,* Reviews of Modern Physics **89**, 1 (2017).

[11] J.-P. Tetienne, L. Rondin, P. Spinicelli, M. Chipaux, T. Debuisschert, J.-F. Roch, and V. Jacques, *Magnetic-field-dependent photodynamics of single NV defects in diamond: an application to qualitative all-optical magnetic imaging,* New Journal of Physics **14**, 103033 (2012).

[12] F. Casola, T. van der Sar, and A. Yacoby, *Probing condensed matter physics with magnetometry based on nitrogen-vacancy centres in diamond,* Nature Reviews Materials **3**, 17088 (2018).

[13] J. Jeske, D. W. Lau, X. Vidal, L. P. McGuinness, P. Reineck, B. C. Johnson, M. W. Doherty, J. C. McCallum, S. Onoda, F. Jelezko, T. Ohshima, T. Volz, J. H. Cole, B. C. Gibson, and A. D. Greentree, *Stimulated emission from nitrogen-vacancy centres in diamond,* Nature Communications **8**, 370 (2017).

[14] A. Gruber, A. Dräbenstedt, C. Tietz, L. Fleury, J. Wrachtrup, and C. Von Borczyskowski, *Scanning confocal optical microscopy and magnetic resonance on single defect centers,* Science **276**, 2012 (1997).

[15] S. Blundell, *Magnetism in Condensed Matter* (Oxford, 2001).

[16] E. Van Oort and M. Glasbeek, *Electric-field-induced modulation of spin echoes of N-V centers in diamond,* Chemical Physics Letters **168**, 529 (1990).

[17] F. Dolde, H. Fedder, M. W. Doherty, T. Nöbauer, F. Rempp, G. Balasubramanian, T. Wolf, F. Reinhard, L. C. Hollenberg, F. Jelezko, and J. Wrachtrup, *Electric-field sensing using single diamond spins,* Nature Physics **7**, 459 (2011).

[18] N. B. Manson, X.-F. He, and P. T. H. Fisk, *Raman heterodyne detected electron-nuclear-double-resonance measurements of the nitrogen-vacancy center in diamond,* Optics Letters **15**, 1096 (1990).

[19] E. R. Macquarrie, T. A. Gosavi, N. R. Jungwirth, S. A. Bhave, and G. D. Fuchs, *Mechanical spin control of nitrogen-vacancy centers in diamond,* Physical Review Letters **111**, 227602 (2013).

[20] P. V. Klimov, A. L. Falk, B. B. Buckley, and D. D. Awschalom, *Electrically driven spin resonance in silicon carbide color centers,* Physical Review Letters **112**, 087601 (2014).

[21] B. A. Myers, A. Ariyaratne, and A. C. Jayich, *Double-Quantum Spin-Relaxation Limits to Coherence of Near-Surface Nitrogen-Vacancy Centers,* Physical Review Letters **118**, 197201 (2017).

[22] P. Neumann, R. Kolesov, V. Jacques, J. Beck, J. Tisler, A. Batalov, L. Rogers, N. B. Manson, G. Balasubramanian, F. Jelezko, and J. Wrachtrup, *Excited-state spectroscopy of single NV defects in diamond using optically detected magnetic resonance,* New Journal of Physics **11**, 013017 (2009).

[23] T. van der Sar, F. Casola, R. Walsworth, and A. Yacoby, *Nanometre-scale probing of spin waves using single-electron spins.* Nature communications **6**, 7886 (2015).

[24] A. Dréau, M. Lesik, L. Rondin, P. Spinicelli, O. Arcizet, J. F. Roch, and V. Jacques, *Avoiding power broadening in optically detected magnetic resonance of single NV defects for enhanced dc magnetic field sensitivity,* Physical Review B **84**, 195204 (2011).

[25] C. P. Slichter, *Principles of Magnetic Resonance* (Springer, 1990).

[26] F. Bloch and A. Siegert, *Magnetic resonance for nonrotating fields,* Physical Review **57**, 522 (1940).

[27] J. Tuorila, M. Silveri, M. Sillanpää, E. Thuneberg, Y. Makhlin, and P. Hakonen, *Stark effect and generalized Bloch-Siegert shift in a strongly driven two-level system,* Physical Review Letters **105**, 257003 (2010).

[28] W. G. Breiland, H. C. Brenner, and C. B. Harris, *Coherence in multilevel systems. I. Coherence in excited states and its application to optically detected magnetic resonance in phosphorescent triplet states ,* Journal of Chemical Physics **62**, 3458 (1975).

[29] F. Jelezko, T. Gaebel, I. Popa, A. Gruber, and J. Wrachtrup, *Observation of Coherent Oscillations in a Single Electron Spin,* Physical Review Letters **92**, 076401 (2004).

[30] J. R. Rabeau, P. Reichart, G. Tamanyan, D. N. Jamieson, S. Prawer, F. Jelezko, T. Gaebel, I. Popa, M. Domhan, and J. Wrachtrup, *Implantation of labelled single nitrogen vacancy centers in diamond using* ^{15}N, Applied Physics Letters **88**, 023113 (2006).

[31] L. Viola, S. Lloyd, and E. Knill, *Universal control of decoupled quantum systems,* Physical Review Letters **83**, 4888 (1999).

[32] F. Jelezko, T. Gaebel, I. Popa, M. Domhan, A. Gruber, and J. Wrachtrup, *Observation of coherent oscillation of a single nuclear spin and realization of a two-qubit conditional quantum gate,* Physical Review Letters **93**, 130501 (2004).

[33] T. Gaebel, M. Domhan, I. Popa, C. Wittmann, P. Neumann, F. Jelezko, J. R. Rabeau, N. Stavrias, A. D. Greentree, S. Prawer, J. Meijer, J. Twamley, P. R. Hemmer, and J. Wrachtrup, *Room-temperature coherent coupling of single spins in diamond,* Nature Physics **2**, 408 (2006).

[34] L. Childress, M. V. Gurudev Dutt, J. M. Taylor, A. S. Zibrov, F. Jelezko, J. Wrachtrup, P. R. Hemmer, and M. D. Lukin, *Coherent dynamics of coupled electron and nuclear spin qubits in diamond,* Science **314**, 281 (2006).

[35] T. Staudacher, F. Shi, S. Pezzagna, J. Meijer, J. Du, C. A. Meriles, F. Reinhard, and J. Wrachtrup, *Nuclear magnetic resonance spectroscopy on a (5-nanometer)3 sample volume,* Science **339**, 561 (2013).

[36] S. J. Devience, L. M. Pham, I. Lovchinsky, A. O. Sushkov, N. Bar-Gill, C. Belthangady, F. Casola, M. Corbett, H. Zhang, M. Lukin, H. Park, A. Yacoby, and R. L. Walsworth, *Nanoscale NMR spectroscopy and imaging of multiple nuclear species,* Nature Nanotechnology **10**, 129 (2015).

[37] I. Lovchinsky, J. D. Sanchez-Yamagishi, E. K. Urbach, S. Choi, S. Fang, T. I. Andersen, K. Watanabe, T. Taniguchi, A. Bylinskii, E. Kaxiras, P. Kim, H. Park, and M. D. Lukin, *Magnetic resonance spectroscopy of an atomically thin material using a single-spin qubit,* Science **355**, 503 (2017).

[38] R. Hanson, V. V. Dobrovitski, A. E. Feiguin, O. Gywat, and D. D. Awschalom, *Coherent dynamics of a single spin interacting with an adjustable spin bath,* Science **320**, 352 (2008).

[39] T. Van Der Sar, Z. H. Wang, M. S. Blok, H. Bernien, T. H. Taminiau, D. M. Toyli, D. A. Lidar, D. D. Awschalom, R. Hanson, and V. V. Dobrovitski, *Decoherence-protected quantum gates for a hybrid solid-state spin register,* Nature **484**, 82 (2012).

[40] M. H. Abobeih, J. Randall, C. E. Bradley, H. P. Bartling, M. A. Bakker, M. J. Degen, M. Markham, D. J. Twitchen, and T. H. Taminiau, *Atomic-scale imaging of a 27-nuclear-spin cluster using a quantum sensor,* Nature **576**, 411 (2019).

[41] B. B. Zhou, P. C. Jerger, K. H. Lee, M. Fukami, F. Mujid, J. Park, and D. D. Awschalom, *Spatiotemporal Mapping of a Photocurrent Vortex in Monolayer MoS2 Using Diamond Quantum Sensors,* Physical Review X **10**, 011003 (2020).

[42] G. De Lange, Z. H. Wang, D. Ristè, V. Dobrovitski, and R. Hanson, *Universal dynamical decoupling of a single solid-state spin from a spin bath,* Science **330**, 60 (2010).

[43] G. De Lange, T. Van Der Sar, M. Blok, Z. H. Wang, V. Dobrovitski, and R. Hanson, *Controlling the quantum dynamics of a mesoscopic spin bath in diamond,* Scientific Reports **2**, 1 (2012).

[44] A. Jarmola, V. M. Acosta, K. Jensen, S. Chemerisov, and D. Budker, *Temperature- and magnetic-field-dependent longitudinal spin relaxation in nitrogen-vacancy ensembles in diamond,* Physical Review Letters **108**, 197601 (2012).

[45] S. Kolkowitz, A. Safira, A. A. High, R. C. Devlin, S. Choi, Q. P. Unterreithmeier, D. Patterson, A. S. Zibrov, V. E. Manucharyan, H. Park, and M. D. Lukin, *Probing Johnson noise and ballistic transport in normal metals with a single-spin qubit,* Science **347**, 1129 (2015).

[46] A. Suter, M. Mali, J. Roos, and D. Brinkmann, *Mixed magnetic and quadrupolar relaxation in the presence of a dominant static Zeeman Hamiltonian,* Journal of Physics: Condensed Matter **10**, 5977 (1998).

[47] B. Flebus and Y. Tserkovnyak, *Quantum-Impurity Relaxometry of Magnetization Dynamics,* Physical Review Letters **121**, 187204 (2018).

[48] S. Chatterjee, J. F. Rodriguez-Nieva, and E. Demler, *Diagnosing phases of magnetic insulators via noise magnetometry with spin qubits,* Physical Review B **99**, 104425 (2019).

[49] A. Rustagi, I. Bertelli, T. Van Der Sar, and P. Upadhyaya, *Sensing chiral magnetic noise via quantum impurity relaxometry,* Physical Review B **102**, 220403 (2020).